

Signal enhancement in spark-assisted laser-induced breakdown spectroscopy for discrimination of glioblastoma and oligodendroglioma lesions

PARISA MOHAMMADIMATIN,¹ PARVIZ PARVIN,^{1,*} AMIR JAFARGHOLI,² AMIN JAHANBAKHSI,³ FATEMEH AHMADINOURI,¹  ALIREZA TABIBKHOEI,⁴ OMID HEIDARI,¹ AND SAREH SALARINEJAD⁵

¹Department of Physics and Energy Engineering, Amirkabir University of Technology, P.O. Box 15875-4413, Tehran, Iran

²Department of Electronic and Electrical Engineering, University College London (UCL), United Kingdom

³Stem Cell and Regenerative Medicine Research Center, Iran University of Medical Sciences, P.O. Box, 1997667665, Tehran, Iran

⁴Skull Base Research Center, Department of Neurosurgery, Iran University of Medical Sciences, P.O. Box, 1997667665, Tehran, Iran

⁵Shohada-e-Tajrish Hospital, Department of Pathology, Faculty of Medicine, Shahid Beheshti University of Medical Sciences, P.O. box 1985717443, Tehran, Iran

*parvin@aut.ac.ir

Abstract: Here, the discrimination of two types of lethal brain cancers, i.e., glioblastoma multiforme (GBM) and oligodendroglioma (OG) are investigated under the laser-induced breakdown spectroscopy (LIBS) and the electrical spark-assisted laser-induced breakdown spectroscopy (SA-LIBS) in order to discriminate the human brain glioma lesions against the infiltrated tissues. It is shown there are notable differences between the plasma emissions over the brain gliomas against those of infiltrated tissues. In fact, a notable enhancement appears in the characteristic emissions in favor of SA-LIBS against those of conventional LIB spectra. Moreover, the plasma properties such as temperature, electron density, and degree of ionization are probed through the data processing of the plasma emissions. The corresponding parameters, taken from SA-LIBS data, attest to be lucidly larger than those of LIBS up to one order of magnitude. In addition, the ionic species such as Mg II characteristic line at 279 nm and CaII emission at 393 nm are notably enhanced in favor of SA-LIBS. In general, the experimental evidence verifies that SA-LIBS is beneficial in the discrimination and grading of GBM/OG neoplasia against healthy (infiltrate) tissues in the early stages.

© 2023 Optica Publishing Group under the terms of the [Optica Open Access Publishing Agreement](#)

1. Introduction

According to the American Cancer Society, in 2022, nearly 25,000 patients will be diagnosed with brain malignancy or other nervous system leading to lethal cases of ~ 18,000 individually. Gliomas are considered central nervous system (CNS) tumors, which account for high occurrence and recurrence rates, with no absolute treatment [1,2]. The tumors originate from the glial cells and spinal cord [3–5]. Gliomas comprise 32% of all primary brain tumors and 80% of the central nervous system malignant tumors. Surgery, radiation, and chemotherapy may extend life, however, not longer than a few years [6].

OG is a diffusely infiltrating glioma that constitutes ~ 5% of primary intracranial tumors [7]. OGs often involve the cortical white matter and are most commonly seen in the frontal lobes [8,9]. These tumors are believed to originate from the oligodendrocytes, whose cells wrap around

nerve cells, acting as a form of electrical insulation against the conduction of nerve impulses [10]. While OG-I and OG-II are benign, OG-III is known as another type of malignant glioma. OGs are usually slow-growing low-grade neoplasms that demonstrate a successful therapy. Grade III anaplastic OG is a malignant form of the tumor having a less favourable prognosis, resulting in rather vast degeneration [11–13]. Low-grade OGs exhibit a median survival time of 10–12 years with overall survival rates of 51–83%, whereas high-grade anaplastic OG attests to a shorter survival time of 3.5 years [11,14,15].

On the other hand, GBM includes over half of the gliomas as the most prevalent case of neoplasia affecting adults [16,17]. GBM is commonly located in the supratentorial region (frontal, temporal, parietal, and occipital lobes) and is rarely located in the cerebellum [16,18]. GBM rapidly grows, leading to death within months. The tumor looks like anaplastic astrocytoma with necrosis areas. The latter arises from the cell's proliferation faster than the growth of new blood vessels to nourish the tumor cells. The malignancy sometimes is characterized by areas of central necrosis and patchy areas of restricted diffusion, which rarely happen in OG [11,14].

Surgery is the current remedy for brain tumors leading to complete tumor removal [2,3]. However, tumor cells often infiltrate surrounding healthy tissues, as the accurate tumor margins are not well-discerned [3,19]. So, the tumor residual negatively affects the therapy process and may cause a high recurrence. Similarly, the inessential removal of healthy functional tissues gives rise to serious neurological defects and irreversible damage to the patient's quality of life [20,21]. Hence, the demand for a suitable diagnostic method would mitigate postoperative nerve damage [21].

Nowadays, brain lesions are usually discriminated through histopathological biopsy and imaging techniques. Computed tomography (CT) and magnetic resonance imaging (MRI), single-photon emission computed tomography (SPECT), and positron emission tomography (PET) are among the routine imaging instruments to reveal tumors [22,23]. It is worth noting that those tools cannot discern the nature of contents at the cellular level. However, in fact, SPECT and PET are not routinely used to diagnose GBM. Clinically, CT is used for the first screening while in principle always gadolinium-enhanced MRI (MRI + contrast) is employed to discern GBM/OG. Diffusion-weighted imaging (DWI), apparent diffusion coefficient (ADC), and more advanced perfusion-weighted MRI technologies (adjunct to contrast-enhanced MRI) do try to distinguish cellular behaviours. The magnetic resonance spectroscopy and PET are not routinely used in practice and mainly remain for research. In general, the global demand requires to search for a fast discrimination technique of cancerous tumors against the infiltrated tissues providing a prompt and non-invasive way of in vivo brain cancer discrimination. Optical methods such as Raman, laser-induced fluorescence spectroscopy (LIF), and LIBS spectroscopy are taken into account as the potentially available techniques [22].

Here, we have focused on LIBS according to the attendance of atomic/ionic species in laser-induced plasma over tissues to discriminate the GBM/OG lesions from the infiltrated tissues. "LIBS" is minimally invasive on the tissue section against the biopsy which is 100% invasive that benefits fast response, real-time, low cost, multi-elemental analysis, and easy operation, avoiding any sample preparation [23,24].

An intense laser shot is focused on the tissue surface. A small portion of tissue is evaporated, initiating an avalanche ionization of the sample elements in the form of a microplasma. An optical fiber coupled spectrometer is used to collect and analyze the characteristic atomic emissions of the induced plasma. The optical emission spectra (OES) contain information regarding the sample characteristics, such as the elemental abundance as well as the corresponding plasma properties. Those parameters are obtained under local thermodynamic equilibrium (LTE) conditions [25–29].

Despite the advantages above, LIBS has some limitations, including poor detection at low pulsed energy; however, using a secondary excitation source can overcome the drawback. It is obvious that LIBS needs a sensitive detector and adequate pulsed energy. We have employed

Avantes, Ava-Spec 2048, 0.4 nm resolution, coupled with an array detector. For this purpose, a combination of LIBS with a secondary excitation source, i.e., a simultaneous electric spark is suggested allowing more intense signals alongside a notable reduction of the required energy per shot leading to less surface damage as well as the elevation of the ionic species as a key parameter for the prompt discrimination. LIBS has been reviewed in cancers diagnosis, classification [30] and quantitative elemental mapping of biological tissues using matrix recognition [31]. Furthermore, all fiber optics system have been recently introduced for the tissue differentiation [32].

This work investigates the discrimination of incurable brain cancers (GBM/OG) under LIBS and SA-LIBS. A Q-switched Nd: YAG laser at 1064 nm is employed as the near-infrared region (NIR) coherent source to induce plasma over the human brain glioma tissues. SA-LIBS exploits the electric discharge (spark) simultaneously to reheat the plasma as a secondary excitation source [33]. Subsequently, the characteristic emissions in the spectra are assessed. These attest that the abundance of trace elements lucidly elevates in favor of cancerous tissues against healthy ones. We do not intend to study tissue layer-by-layer in favor of 3D mapping. 3D elemental mapping is reported frequently by LIBS in literature [34,35]. Here, the line scan in favor of typical CaII and MgII for GBM/infiltrate and OG/infiltrate was carried out alongside the corresponding pathological examination. Furthermore, the plasma parameters such as temperature, electron density, and degree of ionization (DOI) are determined according to the Boltzmann plots, Saha equation, and Stark broadening. In fact, a notable enhancement in characteristic lines is observed using the spark-assisted LIBS against the conventional one. The spectral emission enhancement relies on the plasma temperature, hence its value in SA-LIBS becomes more pronounced with respect to that of LIBS. The early discrimination of GBM/OG based on SA-LIBS deals with trace elements detection by means of rather faint laser shots to avoid lateral damage of healthy tissues. To the best of our knowledge, a few articles are available to investigate LIBS discrimination of GBM/OG tumors [30–32]. Moreover, no one has reported the findings on OG lesions based on techniques of interest. Furthermore, there is no article available utilizing SA-LIBS so far to identify the lethal brain lesions at early stages. Table 1 tabulates previous results on the elemental characteristic emission in brain tumors based on LIBS addressing the notable elevation of calcium and magnesium content in the GBM/OG specimens.

Table 1. Previous results on the elemental characteristic emissions of brain tumors using LIBS

Sample	Aim	Elements	Findings	Ref.
Human Tumors: Glioma, Control: Infiltrate	Discrimination of infiltrative glioma boundary	Ca, Mg, Na, H, N, K, O, C, CN, C ₂	Elevated content of Ca and Mg	[20]
Human Tumors: Glioma, Meningioma, Craniopharyngioma Hemangiopericytoma Control: Infiltrate	Identification of brain tumors	Ca, Mg, Na, H, N, K, O, C, CN, C ₂	Elevated content of Ca and Mg	[36]
Mouse Control: Healthy	Brain elemental imaging	Na, Cu, P, Ca, Mg	Brain tissue is enriched with Cu, P, Mg, Ca	[37]

2. Methods and materials

2.1. Tissue sample preparation

Human brain tissues such as infiltrate (as an alternative to normal tissue), OG-III, and GBM are systematically collected, prepared, and examined. It is worth noting that this project has been carried out under the code of ethics IR.IUMS.REC.1400.392 in Medical University of Iran (Tissue sampling) and Amirkabir University of Technology (Laser spectroscopy). Note that

the human samples are taken from Rasul-Akram hospital, Iran University of Medical sciences. In addition, we have no access to confidential personal information of the patients except their gender, age, and types of infections. The human materials were the archived specimens taken from Rasul-Akram hospital, Iran University of medical sciences, and pathological analyses were performed accordingly. Figure 1 (a, b) shows the typical pathology images for GBM/infiltrate and OG/infiltrate. The tissues were kept in the formalin solution to prevent structure deformation. To perform the experiments, the tissues were cut as $10.5 \text{ mm} \times 10 \text{ mm}$ with $\sim 1 \text{ mm}$ thickness using a microtome, then tissue samples were placed on the glass slides. Tissues were obtained from 5 and 4 patients after the biopsy involved in GBM and OG, respectively. The infiltrated tissues alongside cancerous tumors were taken from the individual organs of each patient. The tumor and surrounding tissues are evaluated together for each tumor and this process is repeated for all samples of interest. The tumor and surrounding tissues are evaluated together for each tumor and this process is repeated for all samples of interest. The data of tumor samples did not merge together, because each patient's tissue is investigated with his/her own control to discriminate tumors from surroundings separately. The LIBS and SA-LIBS were performed separately in a single shot, with 20 shots/sample. Around 20 spectra were obtained from different parts of each tissue. In fact, 20×5 spectra of GBM and 20×4 spectra of OG were totally recorded by the spectrophotometer, and the average spectra were taken from each tissue subsequently. Note that access to archived human material is difficult which took 3 years follow-up.

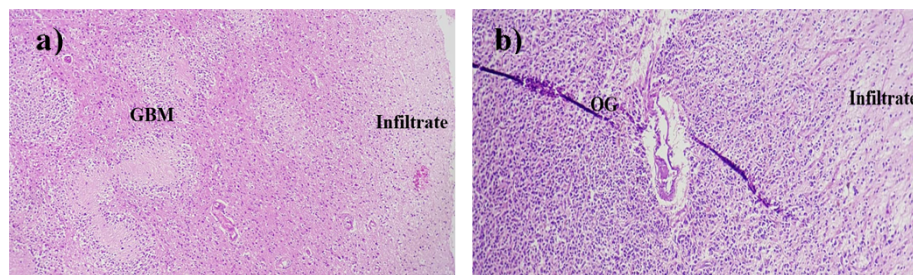


Fig. 1. Histological images of left to right (a) GBM/infiltrate and (b) OG/infiltrate.

2.2. SA-LIBS experimental array

Figure 2 illustrates the LIBS/SA-LIBS experimental setup to collect the laser-induced plasma emissions of the tissue of interest. A Q-switched Nd: YAG laser at 1064 nm with 10 ns pulse width, 50 mJ/pulse, and a pulse repetition rate of 1 Hz is used to generate microplasmas on the samples. The laser beam is focused on the surface through a plano-convex lens with a 20 cm focal length. An optical fiber (FCB-UV400-2-ME-SR) collects the plasma emissions into the spectrometer (Avantes, Ava-Spec 2048, 0.4 nm precision, 200–1100 nm). The fiber tip is positioned 5 cm far from the plasma center at an angle of 45 degrees with respect to the target. The electrode pair, 3.2 mm diameter and 6 cm length, is designed as shown in Fig. 2 with 6 mm spacing at the tip and scan step of 0.5 mm over the target if necessary. In the LIBS technique, the signal acquisition is controlled with the delay time, which is the time between the emission of the laser pulse and the reading of the spectrum, and the gate width, which is the integration time of the spectrometer. To reduce background noise, the delay time is set to 1.2 μs , and the CCD integration time is selected $\sim 2 \text{ msec}$. Regarding the SA-LIBS arrangement, the spark gap is made of two cylindrical tungsten rods of 3.2 mm diameters with a hemisphere-shaped tip angled 45° toward the sample. The circuit consists of a high voltage low inductance 13nF capacitor, a high voltage power supply, a charging resistor, and a couple of electrodes. A homemade power supply (12 kV, 10 mA) is fabricated to generate spark discharges. The voltage difference is

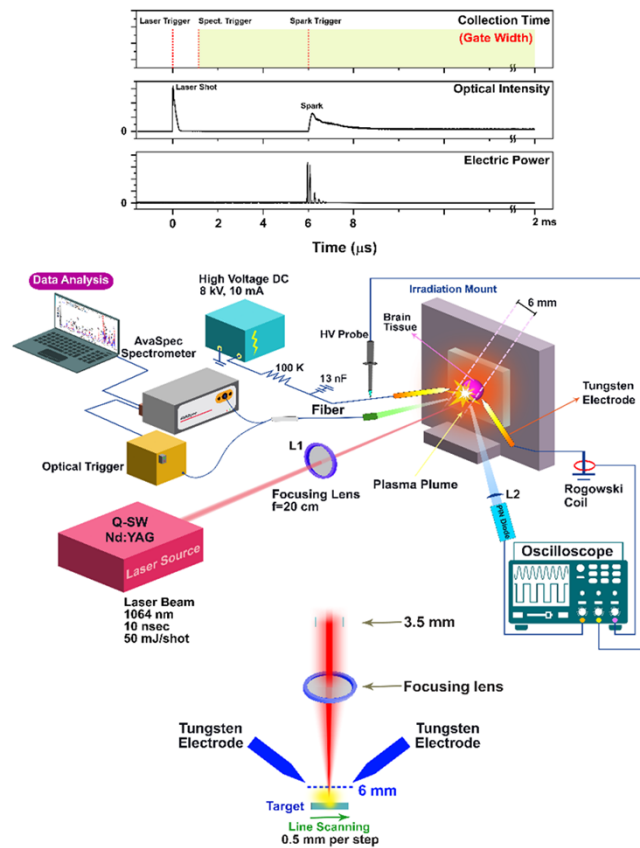


Fig. 2. Schematics of the LIBS/SA-LIBS experimental arrangement to obtain the optical emissions of laserinduced plasmas over the tissue specimens, including several units such as Q-SW Nd: YAG laser, spark generator, digital oscilloscope, spectrometer, an optical trigger, tungsten electrodes, HV probe, and focusing lens. Note that the tungsten (W) electrodes benefit the evaporation temperature much higher than other metals (for instance Ti), so the parasitic W characteristic lines do not appear in the spectra. Time sequence between laser shot, triggering of the spectrometer, and the instant of spark ignition alongside electrical power and the corresponding spark emission: a) sequential trigger, b) light intensity, c) electrical power of the spark emission. According to SA-LIBS an elaborate needle probe is designed with 6 mm gap at the tip using appropriate insulation architecture to elevate more energy to the plasma leading to intense optical emission. The electrode pair, 3.2 mm diameter and 6 cm length are designed with 6 mm spacing at the tip and scan step of 0.5 mm target.

applied across the two electrodes using a homemade variable. The operating voltage of 3 and 5 kV is set during the systematic experiments. The gap between the electrodes is ~ 6 mm, and the spacing between the needle tips and the sample surfaces is kept ~ 4.0 mm. The target is electrically insulated from the stage by placing a piece of a plate [25].

Profilometry is a technique used to extract topographical data from a surface. This can be a single point, a line scan, or even a full 3D scan. The purpose of profilometry is to get the surface morphology, step heights, and surface roughness. This can be done using a physical probe or by means of light. A stylus profilometer is a contact-based one that brings its stylus tip into direct contact measuring surface and traces over the desired path to determine the topography. This

analysis will be supported by the mechanical feedback loop that monitors the force at which the probe moves over the surface of the sample according to the cantilever tip with respect to a specific amount of torque (set point). The changes in the z direction made during the stylus probe tracing over the surface are measured to reconstruct the surface [38]. A Dektak stylus profilometer, model 8000 Veeco, was employed to measure the micro-scale surface alterations with 200 nm vertical resolution [39].

3. Result and discussion

The induced plasma emission spectra are recorded in a series of systematic experiments of LIBS/SA-LIBS on ex-vivo GBM/OG specimens. Several experiments are performed to analyse each sample in favor of LIBS and SA-LIBS using the energy of 50 mJ/shot at an operating voltage of 3 kV and 5 kV. Note that the infiltrated specimens are considered nearly healthy tissues against the malignant ones. Those are excised during a biopsy process around the malignant tumor. Elemental lines and molecular bands are detected over the 200–1100 nm spectral range. For better identification of characteristic emission lines, the spectrum consists of three spectral regions; ultraviolet (UV) (200–450 nm), visible (450–750 nm), and infrared (IR) (750–950 nm). The plasma emission peaks reveal dominant trace elements as excited species C I, Mg I, Ca I, Mn I, Fe I, Na I, Ba I, H_α , H_β , N I, O I, alongside the ionic species of Mg II, Fe II, Ca II, and the molecular CN and C_2 band clusters.

Figure 3 illustrates the emissions over the UV interval due to Mg I (285.21 nm), Mg II (279.52 and 280.35 nm), Mn I (404.20, 417.60 nm), Mn II (257.58 nm), Ca I (422.69 and 443.48 nm), Ca II (315.85, 317.95, 393.38 and 396.86 nm), Fe I (229.80, 358.12, 414.39 nm), Fe II (239.70, 259.92, 274.70 nm), P I (253.35 nm), Na II (305.60 nm), Zn I (330.54, 334.80 nm), and CN bonds cover a spectral range of 385–388 nm. Furthermore, a couple of ionic species, CaII and MgII, mostly appear in the UV region. Figure 4 depicts the average spectra taken by LIBS and SA-LIBS alongside corresponding elemental lines and molecular bands in visible (450–700 nm) spectral regions. The characteristic emissions of Na I (588.99, 589.49 nm), Ca I (616.24 nm), C_2 bonds, as well as H_α (656.28 nm) and H_β (486.16 nm), Ba I (553.25 nm) and Mg I (517.48 nm) are identified in the visible region. Furthermore, H_α and H_β represent humidity, whereas N and O species may come from the atmosphere air. Figure 5 shows the average spectra taken by LIBS/SA-LIBS and corresponding elemental lines as well as molecular bands over the IR spectral region (700–950 nm). The IR spectral region contains K I (766.50, 769.85 nm), and air species constitute such as O I (777.24, 777.42, 777.52, and 844.63 nm) and N I (742.39, 744.25, 746.86, 818.79, 821.65, 824.22, 868.10, 868.36, 868.67, 904.59, and 938.70 nm), N II (463.27, 500.57, 504.56, 545.38, 547.93, 549.58 nm).

Notable differences appear between the plasma emissions of the infiltrate and brain gliomas. Accordingly, there are lucid discrepancies between the relative intensity of the Ba, Mg, Ca, and Fe species in the infiltrate and brain gliomas. Signals are recorded under two discharge voltages of interest. Note that typical ionic species in SA-LIBS elevate with respect to those of LIBS, and the plasma lifetime is notably prolonged. The spectrometer collected more photons, resulting in enhanced spectral intensity in the SA-LIBS arrangement.

The Fe characteristic line is notably higher in GBM/OG than infiltrate ones, which most likely arises from the abnormal growth of blood vessels in malignant tumors leading to the larger blood content. Note that Fe trace at 358.12 nm in hemoglobin is detected in the UV region of OES. The iron trace element plays a role in oxygen transportation and oxidative phosphorylation. The Mn concentration from the line taken at 404.20 nm is larger in the neoplasia lesion than in the infiltrate specimens. manganese (Mn) is taken into account as another significant microelement during cell development. Mn acts as a co-factor of the enzymes regulating the glucose metabolism and other carbohydrates, as well as lipids and proteins synthesis that exhibits critical function in the synthesis of proteoglycans and glycoproteins. It is a crucial component of the formation of bone

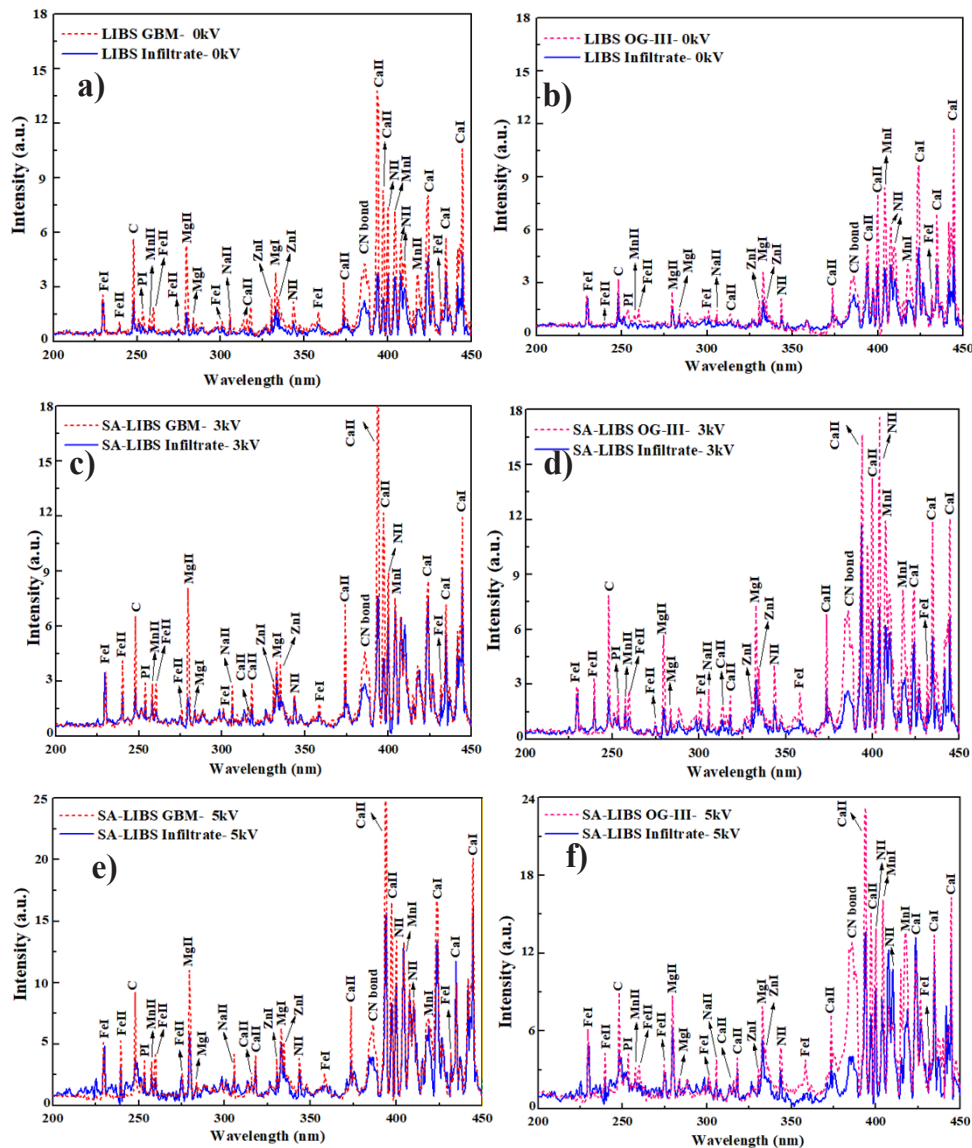


Fig. 3. Average spectra were taken by LIBS and SA-LIBS including corresponding elemental lines and molecular bands in the UV spectral region (200–450 nm). (a) LIBS of infiltrate/GBM, (b) LIBS of infiltrate/OG, (c) SA-LIBS at 3 kV for infiltrate/GBM, (d) SA-LIBS at 3 kV for infiltrate/OG, (e) SA-LIBS at 5 kV for infiltrate/GBM, (f) SA-LIBS at 5 kV for infiltrate/OG human specimens.

and the nervous system. This microelement also contributes to reducing oxidation reactions due to its chemical properties. An example of such a reaction is the superoxide dismutase (MnSOD) activity with Mn as a notable enzyme component. Manganese superoxide dismutase also functions in the differentiating cells [40,41].

Moreover, the elevation in Ca and Mg abundance in the cancerous tissues are pronounced. It is well-known that proliferation depends on the cell cycle, which consists of four primary phases. The transitions between these different phases are tightly controlled, and checkpoints during the

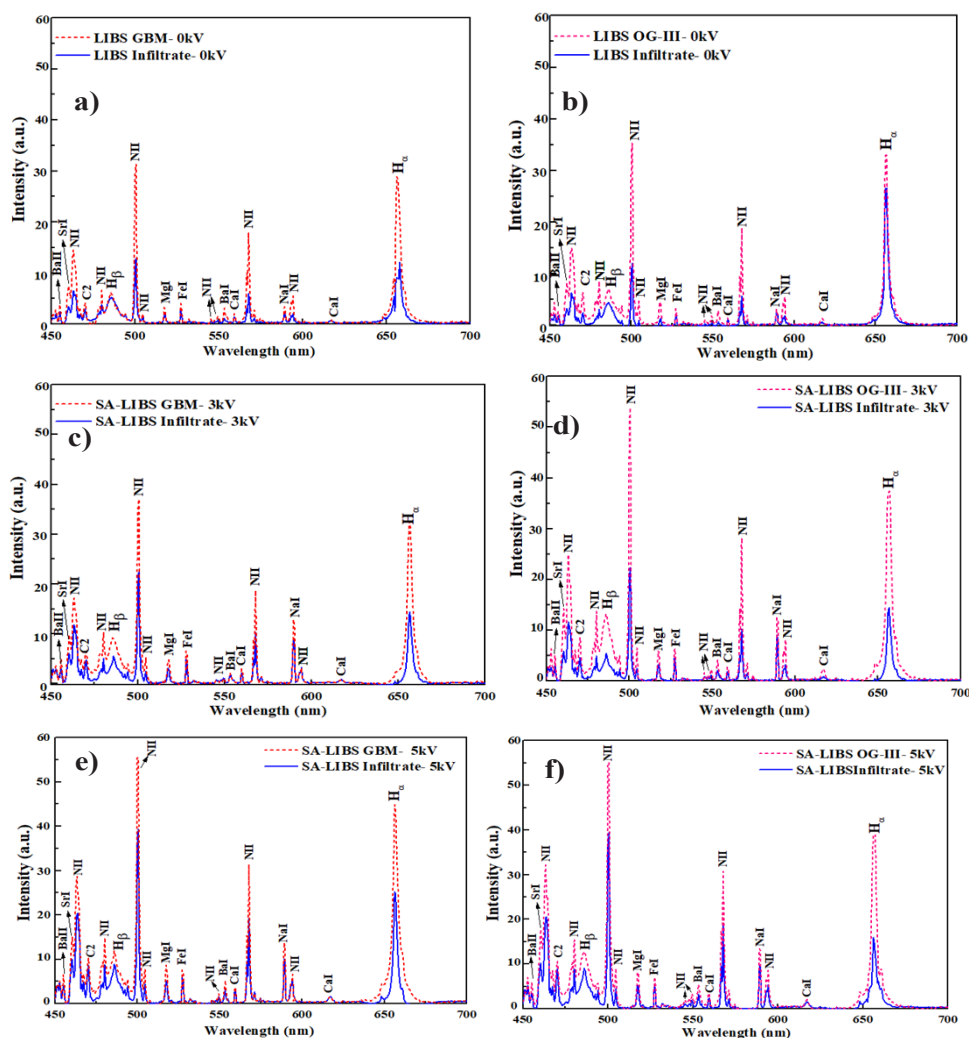


Fig. 4. Average spectra were taken by LIBS and SA-LIBS including corresponding elemental lines and molecular bands in the visible spectral region (450-700 nm). (a) LIBS of infiltrate/GBM, (b) LIBS of infiltrate/OG, (c) SA-LIBS at 3 kV for infiltrate/GBM, (d) SA-LIBS at 3 kV for infiltrate/OG, (e) SA-LIBS at 5 kV for infiltrate/GBM, (f) SA-LIBS at 5 kV for infiltrate/OG human specimens.

cell cycle determine whether the cell proceeds to the next phase [42]. These checkpoints are dependent on calcium as Ca^{+2} is involved in the cell cycle progression and cell proliferation [43,44]. On the other hand, Mg is essential for the infiltration of the physiological and biochemical functions of cells. As a cofactor for over 300 enzymes, they are specifically involved in nucleic acid synthesis and energy metabolism, protein synthesis, cell proliferation, transmembrane ion flux, calcium channel gating, muscle contraction, neuronal activity, and cardiac function, and the release of neurotransmitters [45,46]. Note that $\sim 5\%$ of intracellular magnesium is found in the free ionized form of Mg^{+2} , which can potentially function as a second messenger similar to Ca^{+2} . Among the ionic channels mediating intracellular entry, the transient receptor potential melastatin type7 (TRPM7) channel is of particular interest. This is a non-selective, cationic channel mediating both Ca^{+2} and Mg^{+2} influx. Figure 6 illustrates a schematic diagram of the

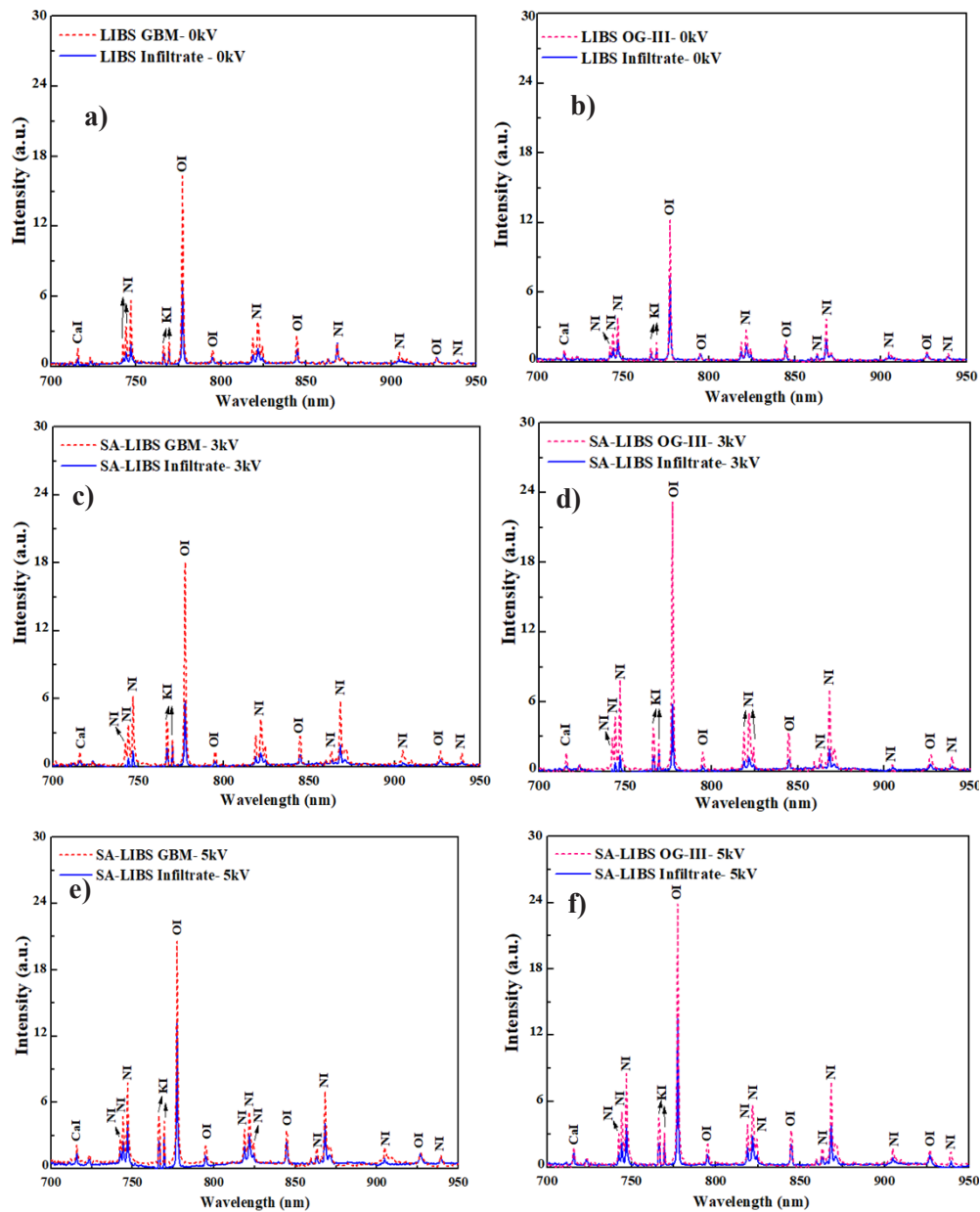


Fig. 5. Average spectra were taken by LIBS and SA-LIBS including corresponding elemental lines and molecular bands in IR spectral region (700-950 nm). (a) LIBS of infiltrate/GBM, (b) LIBS of infiltrate/OG, (c) SA-LIBS at 3 kV for infiltrate/GBM, (d) SA-LIBS at 3 kV for infiltrate/OG, (e) SA-LIBS at 5 kV for infiltrate/GBM, (f) SA-LIBS at 5 kV for infiltrate/OG human specimens.

protein structure of the TRPM7 channel kinase, where the ionic species such as Mg^{+2} and Ca^{+2} remain in equilibrium.

TRPM7 is aberrantly activated in the outbreak of human diseases and cancerous lesions [47,48]. TRPM7 acts in various functional performances during cell proliferation, survival, cell cycle progression, growth, migration, invasion, and epithelial-mesenchymal transition (EMT)

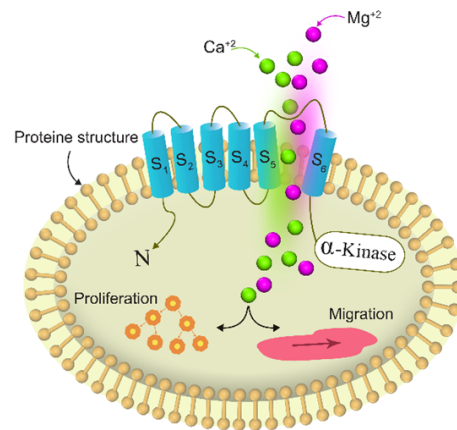


Fig. 6. A schematic diagram to illustrate the protein structure of TRPM7 channel-kinase. The TRPM7 ion channel comprises six transmembrane segments (S1 to S6). The channel pore is located between segments S5 and S6. It is permeable to divalent Mg^{+2} and Ca^{+2} cations that participate in migration, cell proliferation, and EMT. The components of amino-terminal (N-terminal) and carboxy-terminal (C-terminal) embrace the transmembrane segments. TRPM7 is irregularly activated during GBM and OG malignancy.

[47–50]. The ion concentrations relevantly increase in cancerous lesions against the normal cells, which irregularly enhances the ion channels of tissue.

Furthermore, Barium can effectively interact with several EF-hand calcium-binding proteins. This metal ion is also considered as a potent inhibitor of the regulated potassium channels. It can also inactivate some calcium channels. Ba^{2+} activates BK (big potassium) channels, this effect is mediated entirely by action at the Ca^{+2} -bowl site. BK channels are involved in cell cycle regulation and cell proliferation and participated in cell migration and neoplastic of cancer cells, regarding autonomous therapy measures [51,52].

The P characteristic line is notably higher in GBM/OG than in infiltrate ones. The largest abundance of P appears in the deep layers within the cerebellum nearby the middle sagittal plane in the left brain [37]. High phosphorus is required for the rapid growth of the tumor, thus having a role in tumorigenesis and tumor progression. Despite phosphorus being hard to detect by LIBS, the corresponding characteristic line at 253.58 nm is visible using SA-LIBS. Furthermore, Vieira et. al. [33] recently reported spark discharge (SD)-LIBS of fertilizer indicating five P lines at 213.60 nm, 214.90 nm, 215.40 nm, 253.40 nm, and 253.60 nm are hardly revealed whose peaks are very faint during LIBS measurement. This is taken into account as one of the advantages of SA-LIBS against LIBS for P identification. The spectra in Fig. 3 are also in good agreement with the LIBS imaging reported in Fig. 6 of Ref. [36] where the P emission is faint in the brain tissue. Furthermore, the ample species of Ca/Mg obviously appear in the brain based on LIBS, however, P is rare at brain layers in agreement with the present findings. Fig. S.2 shows a typical OG spectra using high(1Å)/low (4 Å) resolution to identify phosphorus line to double-check the elucidation of the P element.

The enhancement of H, C, O, and N characteristic lines occurs in the brain tumoral spectra. These lines arise from a couple of endogenous and exogenous main sources. For instance, the glioma tissue is organic, which accounts for the endogenous source containing C, H, N, and O elements. Conversely, the air is taken as an exogenous source such that H_{α} and H_{β} lines are mainly due to the air humidity, whereas N and O elements address the air constituents. Figure 7 represents typical dominant emission peaks of Ca I (445 nm), Ca II (393 nm), Mg I (518 nm), and Mg II (279 nm) species in OG/ GBM and infiltrate tissues taken by LIBS and SA-LIBS. The

ionic characteristic lines are more intensified against the atomic lines in SA-LIBS. Note that the ionic species such as Mg II and Ca II in SA-LIBS are notably larger than those of LIBS, leading to strong emissions in GBM regarding the OG lesions. The corresponding lines include Ca I at 445 nm, Ca II at 393 nm, Mg I at 518 nm, and Mg II at 279 nm.

Figure 8 (a, c, e, and g) depict the relative signal intensity of the emission in terms of applied voltage for OG-Ca I, OG-Mg I, OG-Ca II, and OG-Mg II, respectively. Furthermore, Fig. 9 (a, c, e, and g) display the relative signal intensity of the emission in terms of applied voltage for GBM-Ca I, GBM-Mg I, GBM-Ca II, and GBM-Mg II, respectively. This attests that peak intensity nonlinearly elevates in terms of the applied voltages. The signal intensity of Ca and Mg emissions attain higher values in favor of the cancerous samples than infiltrated (relatively healthy) tissues. Moreover, Fig. 8 (b, d, f, and h) show the bar graphs addressing the signal enhancement of characteristic emission ratios for OG-Ca I, OG-Mg I, OG-Ca II, and OG-Mg II. Similarly, Fig. 9 (b, d, f, and h) illustrate the bar graphs addressing the signal enhancement of characteristic emission ratios for GBM-Ca I, GBM-Mg I, GBM-Ca II, and GBM-Mg II. The SA-LIBS spectra for both atomic/ionic lines have higher enhancement rates, and the ionic lines intensify more. In fact, Mg II is taken into account as an important factor to discern GBM and OG lesions from each other. Similarly, Ca II is used to identify healthy tissues from GBM/OG lesions. Consequently, OG specimens can be discriminated from GBM ones examining Mg II characteristic emissions at 279 nm. The ionic species such as Mg II and Ca II are lucidly larger in SA-LIBS amplifying GBM emissions regarding OG lesions. Table 2 tabulates uncertainty for the elements in favor of infiltrate and cancerous brain GBM/OG tissues under LIBS/SA-LIBS experiments.

Table 2. Uncertainty for the elements in favor of infiltrate and cancerous brain GBM/OG tissues under LIBS/SA-LIBS experiments.

Type	LIBS %				SA-LIBS (3 kV) %				SA-LIBS (5 kV) %			
	Ca I	Mg I	CaII	Mg II	Ca I	Mg I	CaII	Mg II	Ca I	Mg I	CaII	Mg II
Infiltrate	2.92	5.98	9.82	5.34	4.84	4.38	11.71	8.21	13.33	11.46	9.42	17
OG	10.80	8.45	7.86	6.96	9.64	8.05	8.68	11.04	8.16	6.34	10.55	13.51
GBM	15.70	10.30	14.18	13.58	8.67	7.15	5.71	7.77	9.95	10.69	4.54	5.56

The laser energy pulse can be 15 mJ up to 50 mJ according to the detector properties of Czerny Turner spectrometer and the amount of light collected by the fiber probe as well as the distance of fiber from the target (here 5 cm). The SA-LIBS at 5 kV gives more energy to laser-induced plasma leading to intense characteristic signals. The stylus profilometry is also carried out to demonstrate the crater size. In fact, a typical crater induced by laser in SA-LIBS (5 kV) is shown to visualize the size of ablation and crater diameters. Figure 10 depicts typical stylus profilometry of the crater on brain tissue, a) LIBS at 50 mJ/pulse, V = 0, b) SA-LIBS 5 kV. The spark-assisted LIB does affect negligible change in depth; however, the crater size enlarges in comparison.

3.1. Plasma temperature and electron density

Plasma temperature is recognized as a thermodynamic property due to its ability to prognosis other plasma characteristics, such as the relative populations of energy levels and the speed distribution of particles [54]. The method used during these experiments relies on the Boltzmann plot method assuming LTE is met within the plasma. The temperature of all species in the LTE state is elucidated to be identical. The Boltzmann plot method [55,56] is used to determine the plasma temperature as follows [25,57–59].

$$\ln\left(\frac{I_{ij}\lambda}{g_i A_{ij}}\right) = \ln\left(\frac{n^s}{u^s(T)}\right) - \frac{E_j}{KT}, \quad (1)$$

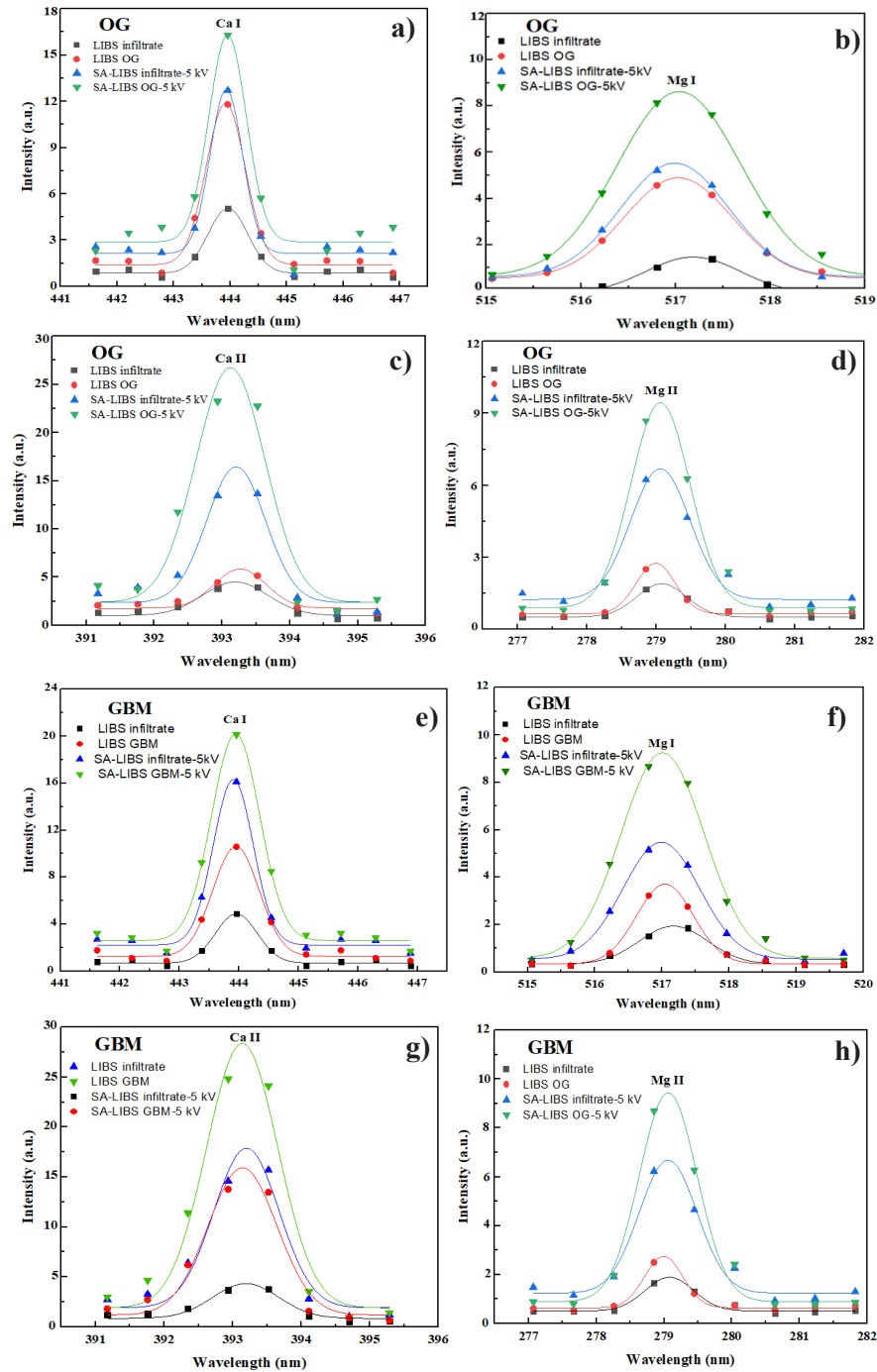


Fig. 7. Typical dominant emission peaks of Ca and Mg in OG, GBM, and infiltrated tissue are taken by LIBS and SA-LIBS, (a) Ca I at 445 nm in OG, (b) Mg I at 518 nm in OG, (c) Ca II at 393 nm in OG, (d) Mg II at 279 nm in OG, (e) Ca I at 445 nm in GBM, (f) Mg I at 518 nm in GBM, (g) Ca II at 393 nm in GBM, (h) Mg II at 279 nm in GBM. A slight spectral shift ($\sim 1 \text{ \AA}$) may be seen among spectral however this is much less than the spectral resolution of the spectrometer (4 \AA) [53]. Note that both data sets and the fitted Gaussian graphs (based on LSM) are depicted together in favor of each characteristic line.

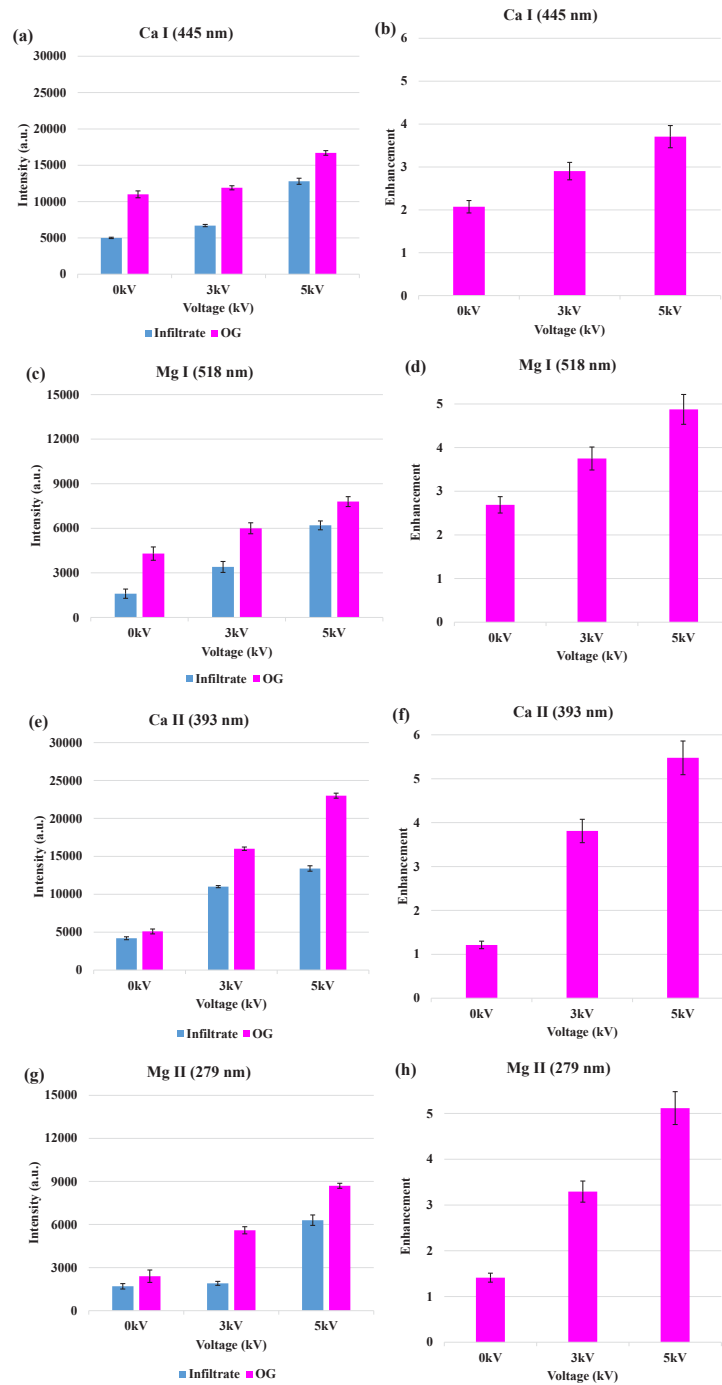


Fig. 8. The relative signal intensity in terms of applied voltages (0, 3, and 5 kV) of the OG (a) Ca I at 445 nm, (c) Mg I at 518 nm, (e) CaII at 393 nm, (g) Mg II at 279 nm, and signal enhancement (ratio of peaks) of atomic and ionic lines, corresponding to LIBS and SA-LIBS of the OG (b) Ca I at 445 nm, (d) Mg I at 518 nm, (f) CaII at 393 nm, (h) Mg II at 279 nm. Note that spectra are recorded for LIBS ($V = 0$) and SA-LIBS ($V = 3$ kV and 5 kV). Note that SD/average values address 20 spectra of sequential shots (20 trials for each voltage). The enhancement values (ratio of peaks) are calculated based on the amplitude of each peak of interest (the emission of certain species) over that of the infiltrate species at $V = 0$.

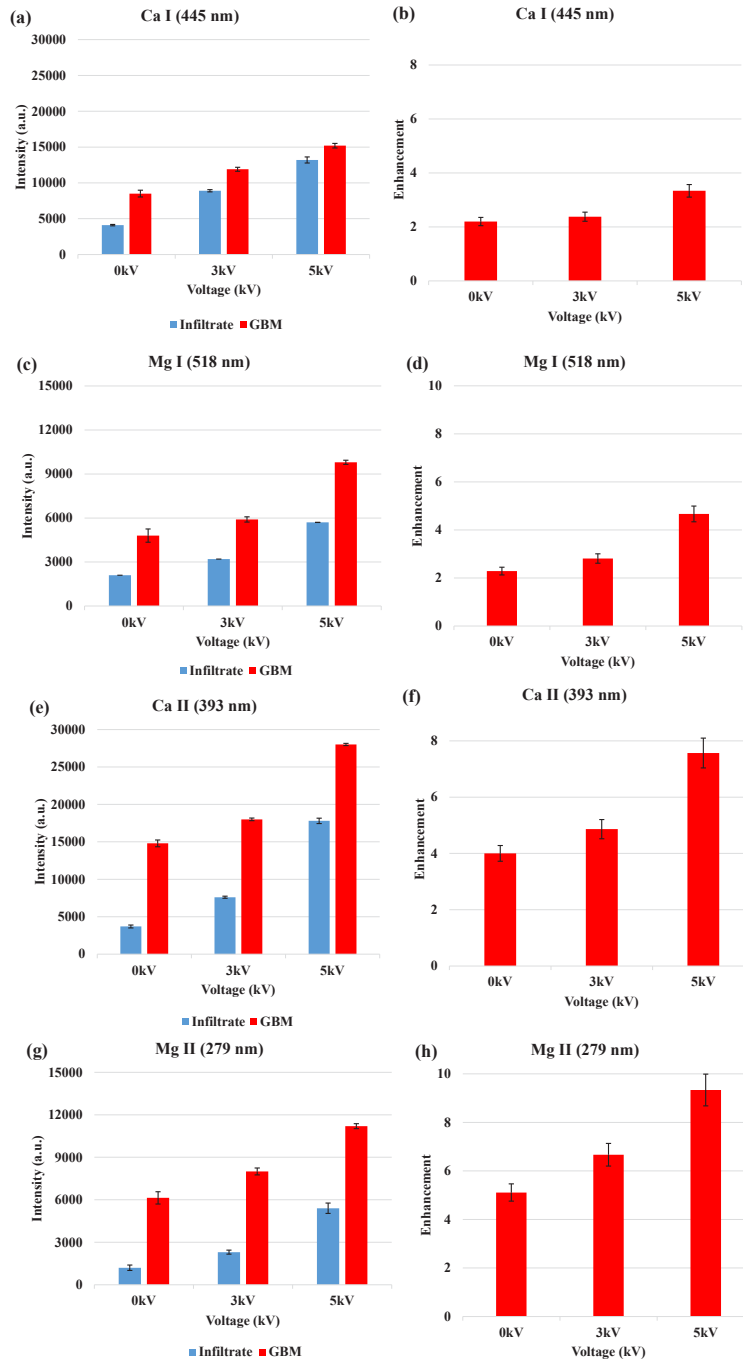


Fig. 9. The relative signal intensity in terms of applied voltages (0, 3, and 5 kV) of the GBM: (a) Ca I at 445 nm, (c) Mg I at 518 nm, (e) CaII at 393 nm, (g) Mg II at 279 nm, and signal enhancement (ratio of peaks) of atomic and ionic lines, corresponding to LIBS and SA-LIBS of the GBM: (b) Ca I at 445 nm, (d) Mg I at 518 nm, (f) CaII at 393 nm, (h) Mg II at 279 nm. Note that spectra are recorded for LIBS ($V = 0$) and SA-LIBS ($V = 3$ kV and 5 kV). Note that SD/average values address 20 spectra of sequential shots (20 trials for each voltage). The enhancement values (ratio of peaks) are calculated based on the amplitude of each peak of interest (the emission of certain species) over that of the infiltrate species at $V = 0$.

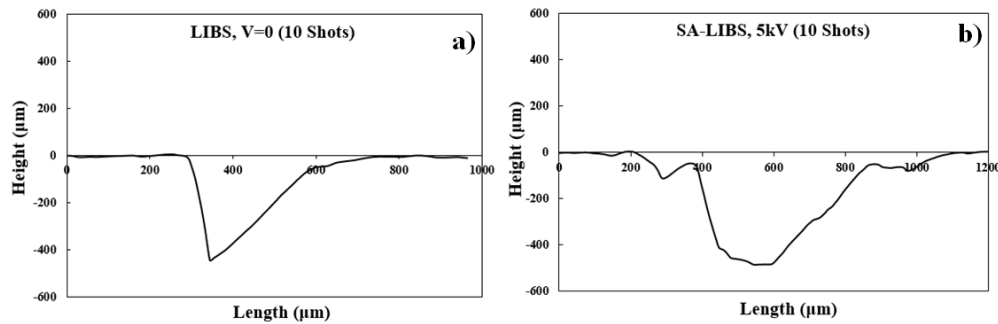


Fig. 10. Typical stylus profilometry of the crater on brain tissue, a) LIBS at 50 mJ/pulse, $V = 0$, b) SA-LIBS 5 kV. Note that ablation in depth takes place with $\sim 40 \mu\text{m}/\text{shot}$. Similarly, the focal laser spot of $\sim 300 \mu\text{m}$ creates an ablative crater in LIBS whereas the size becomes around twice larger in the course of SA-LIBS.

where I_{ij} demonstrates the correction line intensity of the emission line, T_e , g_i , A_{ij} and E_j is the plasma temperature in Kelvin, the level degeneracy for atoms, the transition probability, and the excitation energy of a certain level, respectively. Furthermore, k and n^s indicates the Boltzmann's constant and the total number density of the emitting species in the plasma, respectively. $u^s(T)$ determines the partition function at the plasma temperature T [26,60].

Here, the plasma temperature is determined by examining the relative emission of the Ca species and applying a linear proportion to the experimental data. Figure 11 depicts the Boltzmann plot of the ionic Ca characteristic lines for brain tissues in a series of experiments during LIBS and SA-LIBS (3 and 5 kV) in favor of GBM/OG. The plasma temperatures attest to be notably higher in cancerous tissues than that of corresponding infiltrate characteristic emissions. The data is also analysed via the standard SPSS statistical package to confirm that the temperatures of unhealthy tissues are statistically higher than those of healthy tissues at the 99% confidence level. The corresponding P-values of 0.01 or lower are generally obtained here, emphasizing that certain groups of data are statistically significant and become distinguishable from other groups.

The max temperature difference ΔT between GBM and infiltrate samples exceeds $\sim 1200 \text{ K}$ for SA-LIBS, 5 kV. In addition, SA-LIBS temperatures in OG/GBM/Infiltrate demonstrate notably higher than LIBS data.

Figure 12 represents the plasma temperature of GBM and OG specimens in LIBS and SA-LIBS at LTE conditions [25,61]. Note that $T_{\text{GBM}} > T_{\text{OG}} > T_{\text{infiltrate}}$ and $T_{\text{SA-LIBS}} > T_{\text{LIBS}}$. During cancer progression, the cells lose their original tissue contacts, move through the extracellular matrix (ECM), enter the lymphatic and blood system, extravasate, and ultimately form new tumors. Therefore, tumor cells inevitably experience alterations in cell-cell and cell-ECM adhesion, and the transformation activities of tumor cells are highly influenced by cell adhesion receptors such as cadherins, integrins, cell surface proteoglycans, and tetraspanins. These adhesion receptors, together with extracellular ligands in the tumor microenvironment, couple the extracellular environment to the intracellular signals, thereby enhancing cancer cell migration, proliferation, invasion, and survival [62,63]. Thus cancerous tissue requires smaller laser energy shots to be ablated; hence, more energy imparts to heat plasma, which gives rise to more energetic plasma, enhancing emission signals, and a final plasma temperature rise takes place accordingly.

On the other hand, n_e describes the number of free electrons per unit volume. In addition, the electron density is known as a key plasma parameter according to the LTE criteria. The electron density is assessed by using the Stark broadening of spectral lines. The line broadening in laser-induced plasmas primarily arises from both Doppler and the Stark width.

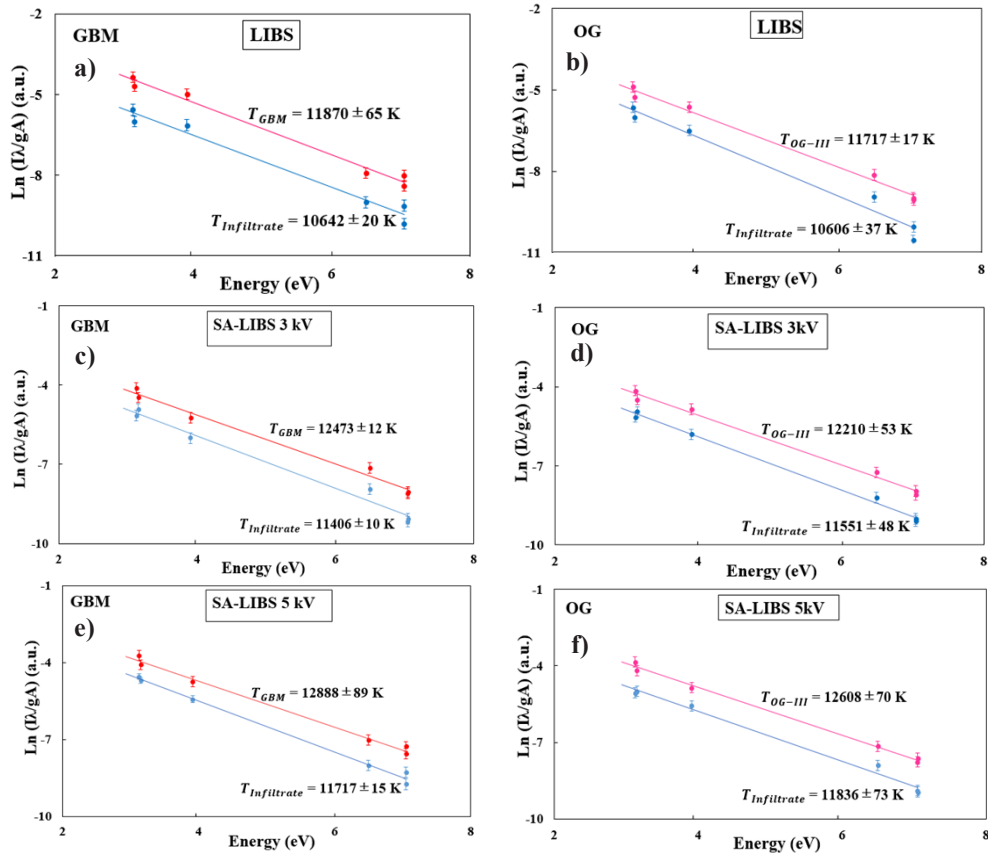


Fig. 11. Boltzmann plots and corresponding plasma temperatures using emission lines of Ca taken from the spectra in LIBS and SA-LIBS (3,5 kV). (a) LIBS infiltrate/GBM, P-value 0.000 (b) LIBS infiltrate/OG, P-value 0.001 (c) SA-LIBS, 3 kV, infiltrate/GBM, P-value 0.009 (d) SA-LIBS, 3 kV, infiltrate/OG, P-value 0.008 (e) SA-LIBS, 5 kV, infiltrate/GBM, P-value 0.005 (f) SA-LIBS, 5 kV, infiltrate/OG, P-value 0.005.

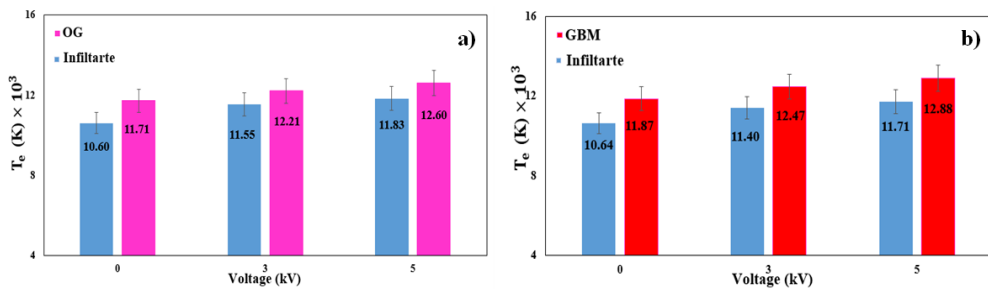


Fig. 12. The plasma temperature of the lesion/infiltrate specimens using SA-LIBS and LIBS arrangements in favor of (a) OG and (b) GBM.

The electron interaction caused Stark broadening, which can be determined as the FWHM (nm) given by [55,64,65]:

$$\nabla\lambda_s = 2W(n_e/10^{16}), \quad (2)$$

where, W denotes the electron impact parameter whereas the contribution of ion broadening was not considered [55,66,67]. The line shapes are frequently fitted with a pure Lorentzian dissemination $\nabla\lambda_{fit}$ mainly due to the Stark impact. The shape of the Gaussian instrumental line ($\nabla\lambda_{ins}$) corresponds to the resolution of the spectrometer, which is determined by measuring the FWHM of the mercury lines emitted by the mercury lamp at low pressure, ~ 0.35 nm. Hence, Lorentzian Stark line width is at that point determined by [55]:

$$\nabla\lambda = (\nabla\lambda_{fit}^2 - \nabla\lambda_{ins}^2)^{\frac{1}{2}} \quad (3)$$

Furthermore, Stark broadening of the trace element lines is used to obtain the electron density of the induced plasma widely, which is determined as [29,56,59,68]:

$$n_e(\text{cm}^{-3}) = 8.2 \times 10^{12} \left(\frac{\nabla\lambda}{\alpha_{1/2}} \right)^{1.5} \quad (4)$$

where, line width $\nabla\lambda$ corresponds to the typical characteristic H_α the line at 656.28 nm and $\alpha_{1/2}$ is a coefficient, which shows a weak dependence on temperature and pressure, to be $\sim 1.86 \times 10^{-2} \text{Å}^\circ$. The characteristic emission of the Balmer line H_α is usually considered to assess the width of the Stark broadening line. On the other hand, the electron density should satisfy the LTE condition given by the McWhirter criterion as [55,65,69]:

$$n_e \geq 1.6 \times 10^{12} T^{0.5} (\nabla E)^3, \quad (5)$$

where, ∇E is the largest interval between adjacent energy levels of the atoms/ions within the plasma in eV. The electron densities are summarized in Table 3, indicating to be more pronounced for the malignant lesions than those of infiltrated tissues. The calculated parameters of n_e are in the order of 10^{17} and properly satisfy the McWhirter criterion to ensure the validity of the LTE criteria. For instance, Eq. (5) is calculated for CaII characteristic lines at 393.38 nm, which gives $n_e \geq 0.5 \times 10^{16} \text{cm}^{-3}$, much lower than the smallest value of n_e obtained in this work.

Table 3. Electron densities and DOI in favor of the infiltrate and cancerous brain GBM/OG tissues in LIBS/SA-LIBS

Tissue type	LIBS				SA-LIBS (3 kV)				SA-LIBS (5 kV)			
	$n_e(\text{cm}^{-3}) \times 10^{17}$		DOI (%)		$n_e(\text{cm}^{-3}) \times 10^{17}$		DOI (%)		$n_e(\text{cm}^{-3}) \times 10^{17}$		DOI (%)	
	Saha	Stark	Saha	Stark	Saha	Stark	Saha	Stark	Saha	Stark	Saha	Stark
Infiltrate/OG	1.10	1.44	0.44	0.57	1.36	2.05	0.54	0.82	1.73	2.11	0.69	0.84
OG	1.89	1.62	0.75	0.65	2.52	2.56	1.00	1.02	3.11	3.28	1.24	1.31
Infiltrate/GBM	1.17	1.60	0.46	0.64	1.70	2.27	0.68	0.91	1.77	2.38	0.71	0.95
GBM	2.02	1.87	0.81	0.75	2.83	3.20	1.13	1.29	3.85	3.40	1.54	1.35

According to Table 3, the differences among the plasma parameters of the infiltrated and cancerous tissues are essential, accounting for key parameters dependent on the compositions and structures of tissues. Many trace elements in malignant tissues are more abundant than those in healthy ones [26]. The initial electron density facilitates the plasma formation of infiltrate/cancerous tissues. In fact, T_e and n_e attest to be notably higher values for cancerous tissues than those in corresponding infiltrates ones, emphasizing more energetic plasma takes place in favor of cancerous tissues. The results elucidate that more abundant trace elements exist in the malignant tissues. The greater ion/atom concentrations in the plasma lead to absorb more photons leading to the stronger inverse Bremsstrahlung (IB) events, which give rise to the extra collisional rates in the plasma plume. Consequently, a larger electron density appears within the plasma. Moreover, the cancerous tissues are easily ablated, and most of the coherent photons are

absorbed in the plasma plume, which in turn undergo a notable temperature rise. Consequently, more energetic plasma takes place leading to higher temperatures and allowing the creation of a larger electron density within the plasma. Similarly, the concentration ratio of the ions to the atomic species can be obtained by manipulation of the Saha-Eggert equation as follows [70,71]:

$$\frac{n_e N_{II}}{N_I} = \frac{g_i g_e (2\pi K m_e T_e)^{1.5} e^{-\frac{E_{ion}}{kT_e}}}{h^3 g_0}, \quad (6)$$

where N_I and N_{II} ascertain to be the number densities of the neutral atomic and singly ionized species, respectively. E_i , n_e , and h are ionization energy, electron density, and Planck's constant, respectively. Furthermore, k , m_e , g_0 , g_e and g_i denote to be Boltzmann's constant, the electron mass, atomic, electron, and ions degeneracy levels, respectively. In the case of weak plasma, the Saha equation deals with $n_e \sim N_{II}$.

In order to determine the electron number density n_e , we can take advantage of charge conservation. If there are n atoms/ions per unit volume, then n_e is written as below:

$$n_e = \frac{N_{II}}{N_{II} + N_I} n, \quad (7)$$

where $N \equiv N_{II} + N_I$. Introducing the ionization fraction $X = \frac{N_{II}}{N}$, which is a function of temperature. Then Eq. (7) is given in the following form [70,71]:

$$\frac{X^2}{1-X} = \frac{1}{n} \frac{g_i g_e (2\pi K m_e T_e)^{1.5} e^{-\frac{E_{ion}}{kT_e}}}{h^3 g_0}. \quad (8)$$

Equation (8) is a quadratic equation in terms of X , that can be solved using standard methods to give out DOI. According to the Saha equation, temperature and electron density are directly related. Hence, the electron density elevates in terms of the temperature and takes on higher values leading to more energetic plasmas.

Table 3 tabulates the values of electron densities and DOI measured in favor of the infiltrate and cancerous brain GBM/OG lesions in the cases of LIBS/SA-LIBS according to Saha and Stark equations. The former is a function of the temperature, while the latter depends on the line width $\nabla\lambda$ that corresponds to the typical characteristic H_α at 656.28 nm. According to Table 3, the results are slightly different using Saha and Stark formalism, that is mainly due to the instrumental errors in the Stark broadening measurements. Eventually, SA-LIBS is focused on the ionic species to achieve more accurate discrimination of lesions.

In general, Table 1 lists the previous studies of LIBS on brain tumors to reveal that a couple of metal elements, i.e., Ca and Mg, could be used to identify glioma against infiltrative healthy boundary tissues. However, detecting the rare Mg trace elements in spectra is difficult and requires alternative assisted techniques [20,36]. The 3D elemental analysis of mouse brain tissue blocks in paraffin was carried out using LIBS, which reports the cortex area is enriched in Ca and Mg. Results suggest LIBS can be exploited as a potential tool for the elemental bioimaging of the whole brain and the ability to improve understanding of complex brain mechanisms in the near future [37]. This work examines SA-LIBS to enhance excited ionic trace elements of brain tissues such as CaII and Mg II. These ionic species are notably elevated in SA-LIBS to strengthen GBM emissions against that of OG lesions. Those are known as notable fingerprints to identify malignant tumors in the early stages whereas LIBS does not.

Fresh tissue contains more water and its absorbance at the laser wavelength is more than that of fixed ex-vivo tissues leading to more heat generation and energetic plasma and extra ablation in comparison. The brain, on the other hand, is made up of soft tissue called grey matter and white matter, which contain neurons and other cells i.e., glial cells that help maintain these neurons. Laser ablation brain surgery is considered as an option for patient brain tumors when

other treatments including radiation therapy have failed and when the tumor is confined to a small, well-defined area.

We hope this technique could find its way into *in vivo* diagnosis using an appropriate biocompatible probe to transfer the laser to the target and collect the spectral emissions. However, a comprehensive dataset and motorizing of the setups could be important to realize *in vivo* study. Minimally invasive diagnosis is based on a portable device which can be implemented to replace the current time-consuming and painful biopsy. LIBS exhibits the potential to be implemented as a diagnostic instrument. Here, our goal is to utilize a clinically inexpensive, real-time feasible method of diagnosis to discriminate cancerous from healthy sites. A broader study needs to inspect *in vivo* experiments; however, it seems that (i) *In vitro/in vivo* trace elements remain invariant; (ii) The ambient body temperature for the *in vivo* condition is $T = 37^{\circ}\text{C}$, while *in vitro* samples are examined at room temperature ($\sim 25^{\circ}\text{C}$) in air; (iii) The live tissues are usually surrounded by wet and viscous media, whereas *in vitro* samples are not so and are usually tested in dry air; and (iv) The induced plasma is confined inside the body tissues. Thus, we believe that *in vivo* plasma properties are elevated because of these indications to scale up the diagnostic power with respect to those obtained in *in vitro* experiments [60].

In general, it is empirically shown that more energetic plasma is created on cancerous tissue surfaces due to the intense atomic/ionic characteristic emissions of species as well as higher electron density. In fact, the clinical approach of LIBS may be realized regarding these findings relying on the spectroscopic instrument equipped with an elaborate needle probe. Eventually, hematoxylin and eosin (H&E) is one of the principal tissue stains widely used in histology for the medical diagnosis and is often called the gold standard. Despite the latter being a sluggish method, however here a rapid way of cancer diagnosis is developed. In fact, H&E is unable to provide a trace element profile across the tissue of interest, whereas the 3D SA-LIBS elemental mapping will be realized as the complement of the gold standard in the near future.

4. Conclusion

This work is a continuation of our previous findings on LIBS of several cancerous tumors to achieve a fast and real-time discrimination. Here, we have developed spark-assisted laser-induced breakdown spectroscopy to discriminate cancerous tissues in their early stages by enhancing the ionic/atomic characteristic emissions of Ca/Mg species. There are distinct discrepancies in the relative intensity of the characteristic emissions of the excited species such as Ca, Mg, Ba, Fe, and Mn within laser-induced plasma over the infiltrate and brain glioma specimens. Furthermore, the spectral intensity enhancement systematically takes place based on spark discharge-assisted LIBS. During SA-LIBS, the plasma lifetime prolongs, leading to more photon collection by the spectrometer and a notably spectral intensity enhancement. The plasma temperature, electron density, and degree of ionization attest to be notably higher in GBM (typically 12888 K, $3.40 \times 10^{17} \text{ cm}^{-3}$, 1.35%, respectively) than OG (typically 12608 K, $3.28 \times 10^{17} \text{ cm}^{-3}$, 1.31%, respectively), according to Fig. 10 and Table 3, while lower values are determined for the infiltrate tissues. Note that ionic species in LIBS are usually rare due to their faint signals. However, MgII and CaII are notably intensified using SA-LIBS. The ionic emission peak is taken into account as the significant footprint of early brain discrimination with the assistance of SA-LIBS. In fact, MgII is used to discern GBM and OG lesions. Similarly, CaII is beneficial to identify healthy tissues from GBM/OG lesions.

The ion concentrations relevantly increase in cancerous lesions against the normal cells, which irregularly enhances the ion channels of tissue. TRPM7 is a non-selective, cationic channel mediating both Ca^{+2} and Mg^{+2} influx. It is aberrantly activated in the outbreak of abnormal cell proliferation. TRPM7 acts in various functional performances during cell proliferation, survival, cell cycle progression, growth, migration, invasion, and epithelial-mesenchymal transition (EMT). At low energy per shot, the laser just ablates the sample, and no intense plasma is created, while

the synchronous spark imparts more energy to heat the vaporized plume creating more energetic plasma and consequently higher plasma temperature appears. This gives rise to reducing the ablation mass alongside creating an intense plasma, essential for sensitive and minimally invasive brain tissue discrimination. The aim is to develop simultaneous discrimination /treatment of lethal brain tumors for minimal lateral damage to healthy tissues.

Acknowledgment. We appreciate Dr. Mohammad Barbarestani from the School of Medicine at Tehran University of Medical Sciences for his collaboration and useful discussions. In addition, we thank Dr. Mahdi Habibpour, for his kind technical advice on spark generator and insulation.

Disclosures. The authors declare no conflicts of interest.

Data availability. Data underlying the results presented in this paper are not publicly available at this time but may be obtained from the authors upon reasonable request.

Supplemental document. See [Supplement 1](#) for supporting content.

References

1. P. Liao, J. L. Finlay, and D. S. Stearns, *et al.*, "Alex's Lemonade Stand Foundation Infant and Childhood Primary Brain and Central Nervous System Tumors Diagnosed in the United States," *Neuro-Oncology* **17**(suppl 5), v29.2–v29 (2015).
2. Y. Zhou, CH. Liu, and B. Wu, *et al.*, "Molecular biomarkers characterization for human brain glioma grading using visible resonance Raman spectroscopy," *APL Photonics* **3**(12), 120802 (2018).
3. H. Mehdine, A. Chalumeau, and F. Poulon, *et al.*, "Optical signatures derived from deep UV to NIR excitation discriminates healthy samples from low and high grades glioma," *Sci. Rep.* **9**(1), 8786 (2019).
4. D. N. Louis, D. Schiff, and T. Batchelor, *et al.*, "Classification and pathologic diagnosis of gliomas," *Up to Date* (Wolters Kluwer Health, 2017).
5. S. Chatterjee, F. A. Nizamani, and A. Nürnberger, *et al.*, "Classification of brain tumours in MR images using deep spatiotemporal models," *Sci. Rep.* **12**(1), 1505 (2022).
6. J. Depciuch, B. Tolpa, and P. Witek, *et al.*, "Raman and FTIR spectroscopy in determining the chemical changes in healthy brain tissues and glioblastoma tumor tissues," *Spectrochim. Acta, Part A* **225**, 117526 (2020).
7. Q. T. Ostrom, H. Gittleman, and C. Kruchko, *et al.*, "Primary brain and other central nervous system tumors in Appalachia: regional differences in incidence, mortality, and survival," *J. Neuro-Oncol.* **142**(1), 27–38 (2019).
8. M. Ahadi, A. Moradi, and A. Rakhshan, *et al.*, "Basic Characteristics of Oligodendrogliomas at the Shohada-e Tajrish Hospital (2008 to 2014)," *Iranian Journal of Pathology* **12**(3), 241–247 (2017).
9. K. K. Koeller and E. J. Rushing, "Oligodendroglioma and its variants: Radiologic-pathologic correlation," *Radiographics* **25**(6), 1669–1688 (2005).
10. P. Göttle, J. K. Sabo, and A. Heinen, *et al.*, "Oligodendroglial maturation is dependent on intracellular protein shuttling," *J. Neurosci.* **35**(3), 906–919 (2015).
11. M. D. Anderson and M. R. Gilbert, "Treatment recommendations for anaplastic oligodendrogliomas that are codeleted," *Oncology* **27**(4), 315 (2013).
12. A. H. Vo, P. Ambady, and D. Spencer, "The IDH1 inhibitor ivosidenib improved seizures in a patient with drug-resistant epilepsy from IDH1 mutant oligodendroglioma," *Epilepsy & Behavior Reports* **18**, 100526 (2022).
13. G. Simonetti, P. Gaviani, and A. Botturi, *et al.*, "Clinical management of grade III oligodendroglioma," *Cancer Manage. Res.* **7**, 213 (2015).
14. C. A. Tork and C. Atkinson, "Oligodendroglioma," [Internet] (Statpearls, 2021).
15. C. J. Kinslow, A. L. Garton, and A. L. Rae, *et al.*, "Extent of resection and survival for oligodendroglioma: a US population-based study," *J. Neuro-Oncol.* **144**(3), 591–601 (2019).
16. F. Hanif, K. Muzaffar, and K. Perveen, *et al.*, "Glioblastoma multiforme: a review of its epidemiology and pathogenesis through clinical presentation and treatment," *Asian Pacific journal of cancer prevention: APJCP* **18**(1), 3 (2017).
17. S. Agnihotri, K. E. Burrell, and A. Wolf, *et al.*, "Glioblastoma, a brief review of history, molecular genetics, animal models and novel therapeutic strategies," *Arch. Immunol. Ther. Exp.* **61**(1), 25–41 (2013).
18. A. F. Tamimi and M. Juweid, "Epidemiology and outcome of glioblastoma," (Exon Publications, 2017) pp.143–153.
19. V. Pirro, C. M. Alfaro, and A. K. Jarmusch, *et al.*, "Intraoperative assessment of tumor margins during glioma resection by desorption electrospray ionization-mass spectrometry," *Proc. Natl. Acad. Sci. U.S.A.* **114**(26), 6700–6705 (2017).
20. Q. W. Geer Teng, H. Zhang, and W. Xiangli, *et al.*, "Discrimination of infiltrative glioma boundary based on laserinduced breakdown spectroscopy," *Spectrochim. Acta, Part B* **165**, 105787 (2020).
21. P. Butte and A. N. Mamelak, "Time-Resolved Laser Induced Fluorescence Spectroscopy (TRLIFS): A tool for intra-operative diagnosis of brain tumors and maximizing extent of surgical resection," in *Tumors of the Central Nervous System*, Volume 5: Springer, 2012, pp. 161–172.
22. Y. Zhou, L. Wang, and C. H. Liu, *et al.*, "Differentiation of cancerous and normal brain tissue using label free fluorescence and stokes shift spectroscopy," in *Optical Biopsy XIV: Toward Real-Time Spectroscopic Imaging and Diagnosis*, 2016, vol. 9703, International Society for Optics and Photonics, p. 97030Q.

23. S. Mortazavi, P. Parvin, and M. M. Pour, *et al.*, "Time-resolved evolution of metal plasma induced by Q-switched Nd: YAG and ArF-excimer lasers," *Opt. Laser Technol.* **62**, 32–39 (2014).
24. S. Z. Mortazavi, P. Parvin, and A. Reyhani, *et al.*, "Generation of various carbon nanostructures in water using IR/UV laser ablation," *J. Phys. D: Appl. Phys.* **46**(16), 165303 (2013).
25. M. Habibpour, P. Parvin, and R. Amrollahi, *et al.*, "Signal Enhancement in Spark-assisted vs. Dual-beam Laser-induced Breakdown Spectroscopy," *At. Spectrosc.* **42**(4), 175–182 (2021).
26. F. Ghasemi, P. Parvin, and J. Reif, *et al.*, "Laser induced breakdown spectroscopy for the diagnosis of several malignant tissue samples," *J. Laser Appl.* **29**(4), 042005 (2017).
27. D. A. Cremers and L. J. Radziemski, *Handbook of Laser-induced Breakdown Spectroscopy* (John Wiley & Sons, 2013).
28. H. Liu, B. S. Truscott, and M. N. Ashfold, "Determination of Stark parameters by cross-calibration in a multi-element laser-induced plasma," *Sci. Rep.* **6**(1), 1–9 (2016).
29. P. Parvin, S. Shoursheini, and F. Khalilnejad, *et al.*, "Simultaneous fluorescence and breakdown spectroscopy of fresh and aging transformer oil immersed in paper using ArF excimer laser," *Optics and Lasers in Engineering* **50**(11), 1672–1676 (2012).
30. M. N. Khan, Q. Wang, and B. S. Idrees, *et al.*, "A review on laser-induced breakdown spectroscopy in different cancers diagnosis and classification," *Front. Phys.* **10**, 10 (2022).
31. P. Janovsky, A. Kéri, and D. J. Palásti, *et al.*, "Quantitative elemental mapping of biological tissues by laser-induced breakdown spectroscopy using matrix recognition," *Sci. Rep.* **13**(1), 10089 (2023).
32. H. Abbasi, R. Guzman, and P. C. Cattin, *et al.*, "All-fiber-optic LIBS system for tissue differentiation: A prospect for endoscopic smart laser osteotomy," *Optics and Lasers in Engineering* **148**, 106765 (2022).
33. A. L. Vieira, T. V. Silva, and F. S. de Sousa, *et al.*, "Determinations of phosphorus in fertilizers by spark discharge-assisted laser-induced breakdown spectroscopy," *Microchem. J.* **139**, 322–326 (2018).
34. K. Kiss, A. Šindelářová, and L. Krbal, *et al.*, "Imaging margins of skin tumors using laser-induced breakdown spectroscopy and machine learning," *J. Anal. At. Spectrom.* **36**(5), 909–916 (2021).
35. A. Limbeck, L. Brunnbauer, and H. Lohninger, *et al.*, "Methodology and applications of elemental mapping by laser induced breakdown spectroscopy," *Anal. Chim. Acta* **1147**, 72–98 (2021).
36. G. Teng, Qianqian Wang, and Haifeng Yang, *et al.*, "Pathological identification of brain tumors based on the characteristics of molecular fragments generated by laser ablation combined with a spiking neural network," *Biomed. Opt. Express* **11**(8), 4276–4289 (2020).
37. Q. Lin, S. Wang, and Y. Duan, *et al.*, "Ex vivo three-dimensional elemental imaging of mouse brain tissue block by laser-induced breakdown spectroscopy," *J. Biophotonics* **14**(5), e202000479 (2021).
38. J. Ružbarský, "The difficulty of measuring the roughness of glossy surfaces using the triangulation principle," *Appl. Sci.* **13**(8), 5155 (2023).
39. S. Shoursheini, P. Parvin, and B. Sajad, *et al.*, "Dual-laser-beam-induced breakdown spectroscopy of copper using simultaneous continuous wave CO₂ and Q-switched Nd: YAG lasers," *Appl. Spectrosc.* **63**(4), 423–429 (2009).
40. B. Florianczyk, R. Kaczmarczyk, and J. Osuchowski, *et al.*, "Metallothionein and manganese concentrations in brain tumors," *Journal of Pre-Clinical and Clinical Research* **1**(1), 89 (2007).
41. K. Cilliers, C. J. Muller, and B. J. Page, "Trace element concentration changes in brain tumors: a review," *The Anatomical Record* **303**(5), 1293–1299 (2020).
42. K. Vermeulen, D. R. Van Bockstaele, and Z. N. Berneman, "The cell cycle: a review of regulation, deregulation and therapeutic targets in cancer," *Cell proliferation* **36**(3), 131–149 (2003).
43. C. R. Kahl and A. R. Means, "Regulation of cell cycle progression by calcium/calmodulin-dependent pathways," *Endocrine reviews* **24**(6), 719–736 (2003).
44. T. Capiod, "Cell proliferation, calcium influx and calcium channels," *Biochimie* **93**(12), 2075–2079 (2011).
45. M. Bara, A. Guiet-Bara, and J. Durlach, "Regulation of sodium and potassium pathways by magnesium in cell membranes," *Magnesium Research* **6**(2), 167–177 (1993).
46. F. I. Wolf, S. Fasanella, and B. Tedesco, *et al.*, "Regulation of magnesium content during proliferation of mammary epithelial cells (HC-11)," *Front Biosci* **9**(1-3), 2056 (2004).
47. N. S. Yee, "Role of TRPM7 in cancer: potential as molecular biomarker and therapeutic target," *Pharmaceuticals* **10**(4), 39 (2017).
48. W. L. Chen, B. A. arszczuk, and E. Turlova, *et al.*, "Inhibition of TRPM7 by carvacrol suppresses glioblastoma cell proliferation, migration and invasion," *Oncotarget* **6**(18), 16321–16340 (2015).
49. N. Déliot and B. Constantin, "Plasma membrane calcium channels in cancer: Alterations and consequences for cell proliferation and migration," *Biochimica et Biophysica Acta (BBA)-Biomembranes* **1848**(10), 2512–2522 (2015).
50. L. Liu, N. Wu, and Y. Wang, *et al.*, "TRPM7 promotes the epithelial–mesenchymal transition in ovarian cancer through the calcium-related PI3K/AKT oncogenic signaling," *J. Exp. Clin. Cancer Res.* **38**(1), 1–15 (2019).
51. Y. Zhou, X.-H. Zeng, and C. J. Lingle, "Barium ions selectively activate BK channels via the Ca²⁺-bowl site," *Proc. Natl. Acad. Sci.* **109**(28), 11413–11418 (2012).
52. Y. Zhou, X. Zeng, and C. J. Lingle, "Barium Ions Selectively Activate BK Channels through the Ca²⁺-Bowl Site," *Biophys. J.* **102**(3), 683a (2012).
53. A. Niazi, P. Parvin, and A. Jafargholi, *et al.*, "Discrimination of normal and cancerous human skin tissues based on laser-induced spectral shift fluorescence microscopy," *Sci. Rep.* **12**(1), 20927 (2022).

54. M. L. Najarian and R. C. Chinni, "Temperature and electron density determination on Laser-Induced Breakdown Spectroscopy (LIBS) plasmas: A physical chemistry experiment," *J. Chem. Educ.* **90**(2), 244–247 (2013).
55. S. Shoursheini, B. Sajad, and P. Parvin, "Determination of gold fineness by laser induced breakdown spectroscopy with the simultaneous use of CW-CO₂ and Q-SW Nd: YAG lasers," *Optics and lasers in engineering* **48**(1), 89–95 (2010).
56. A. Moosakhani, P. Parvin, and S. Z. Mortazavi, *et al.*, "Effect of hydrocarbon molecular decomposition on palladium-assisted laser-induced plasma ablation," *Appl. Opt.* **56**(11), E64–E71 (2017).
57. Y. Wu, T. Sizyuk, and N. Termini, *et al.*, "Spectroscopic studies of laser produced Bi-Pb alloy plasma," *Spectrochim. Acta, Part B* **175**, 106033 (2021).
58. J. R. Dos Santos, J. J. Neto, and N. Rodrigues, *et al.*, "Measurement of Dysprosium Stark Width and the Electron Impact Width Parameter," *Appl. Spectrosc.* **73**(2), 203–213 (2019).
59. M. Al-Salihi, R. Yi, and S. Wang, *et al.*, "Quantitative laser-induced breakdown spectroscopy for discriminating neoplastic tissues from non-neoplastic ones," *Opt. Express* **29**(3), 4159–4173 (2021).
60. F. Ghasemi, P. Parvin, and N. S. H. Motlagh, *et al.*, "Laser induced breakdown spectroscopy and acoustic response techniques to discriminate healthy and cancerous breast tissues," *Appl. Opt.* **55**(29), 8227–8235 (2016).
61. M. Hassanimatin and S. Tavassoli, "Experimental investigation of effective parameters on signal enhancement in spark assisted laser induced breakdown spectroscopy," *Phys. Plasmas* **25**(5), 053302 (2018).
62. M. Janiszewska, M. C. Primi, and T. Izard, "Cell adhesion in cancer: Beyond the migration of single cells," *J. Biol. Chem.* **295**(8), 2495–2505 (2020).
63. M. Anguiano, X. Morales, and C. astilla, *et al.*, "The use of mixed collagen-Matrigel matrices of increasing complexity recapitulates the biphasic role of cell adhesion in cancer cell migration: ECM sensing, remodeling and forces at the leading edge of cancer invasion," *PloS one* **15**(1), e0220019 (2020).
64. H. Griem, "Spectral line broadening by plasmas," *Pure and Applied Physics* **39**, 421 (1974).
65. Y. Zhang, Z. Zhao, and T. Xu, *et al.*, "Characterization of local thermodynamic equilibrium in a laser-induced aluminum alloy plasma," *Appl. Opt.* **55**(10), 2741–2747 (2016).
66. P. Yaroshchik, D. Body, and R. J. Morrison, *et al.*, "A semi-quantitative standard-less analysis method for laser-induced breakdown spectroscopy," *Spectrochim. Acta, Part B* **61**(2), 200–209 (2006).
67. J. Bengoechea, J. Aguilera, and C. Aragón, "Application of laser-induced plasma spectroscopy to the measurement of Stark broadening parameters," *Spectrochim. Acta, Part B* **61**(1), 69–80 (2006).
68. H. Griem, *Spectral Line Broadening by Plasmas* (Academic Press, 1974).
69. G. Cristoforetti, A. De Giacomo, and M. Dell'Aglia, *et al.*, "Local thermodynamic equilibrium in laser-induced breakdown spectroscopy: beyond the McWhirter criterion," *Spectrochim. Acta, Part B* **65**(1), 86–95 (2010).
70. M. Habibpour, P. Parvin, and R. Amrollahi, "Gold fineness measurement using single-shot spark assisted laser-induced breakdown spectroscopy," *Appl. Opt.* **60**(5), 1099–1109 (2021).
71. B. Farcy, R. Arevalo, and M. Taghioskoui, *et al.*, "A prospective microwave plasma source for in situ spaceflight applications," *J. Anal. At. Spectrom.* **35**(11), 2740–2747 (2020).